Radio Science, Volume 33, Number 3, Pages 697–706, May–June 1998

Ground-based radiometric measurements of atmospheric brightness temperature and water contents in Italy

F. Barbaliscia, E. Fionda, and P. G. Masullo
Fondazione Ugo Bordoni, Rome, Italy

Abstract. This paper presents the results of the analysis carried out of ground-based zenith measurements of atmospheric brightness temperature acquired by a dual-channel radiometer at 23.8 and 31.4 GHz at Rome, Italy, uninterruptedly during 4 years, from 1992 to 1996. The cumulative distributions of the atmospheric brightness temperature, as well as of the total water vapor and liquid water contents retrieved via the inversion of radiometric measurements, are presented and discussed. The analysis is performed for various time bases: years, months, and hours of the day, allowing indications of both design parameters and meteorological aspects. Comparison is made of the radiometric data with those calculated on the basis of long-term radiosonde profiles by means of current literature models. Model-oriented analysis is also attempted concerning the separate contributions of the two individual water phases and the possibility of deriving the status of the sky from the measured brightness temperature.

1. Introduction

Radiometry is a passive remote sensing technique related to the measurement of the incoherent electromagnetic energy naturally emitted by all material media. Since this emission behaves as a wideband incoherent signal similar, in both magnitude and features, to the noise generated by the measuring system itself, radiometric measurements are quite delicate in terms of accuracy.

In radio propagation studies, where data on slant links are typically provided by beacon measurements, radiometry is an alternative approach to estimating attenuation, making use of physical characteristics of atmospheric constituents to infer attenuation. While in K_u bands the use of radiometry is limited to rain attenuation, above some 20 GHz the absorption caused by atmospheric minor components, such as gases and clouds, can be related, under proper hypotheses, to radiometric measurements, allowing the evaluation of the path attenuation and the retrieval of the atmospheric total vapor and liquid water contents, by means of which the attenuation can be estimated at other frequencies.

The atmospheric attenuation in the absence of rain is relevant to the design of low-margin satellite communication systems, and the atmospheric water content has impact on several meteorological and environmental aspects, and for estimating the tropospheric path delay, used in radio astronomy applications (very long baseline interferometry), radar altimetry, and satellite-based positioning systems (Global Positioning System (GPS)). In this paper, radiometric measurements of the atmospheric brightness temperature are presented and analyzed with regard to both statistical aspects and the features of the relevant water contents.

Copyright 1998 by the American Geophysical Union.

Paper number 97RS02619.
0048-6604/98/97RS-02619$11.00

2. The Atmospheric Radiative Process

The atmospheric brightness temperature is related to the vertical profiles of the atmospheric physical temperature and absorption through the radiative transfer equation (RTE), which involves both absorption and scattering processes and leads, in the general case, to highly complicated formulations that drastically simplify when scattering may be neglected, that is, at microwave frequencies, in the absence of liquid. When clouds or rain are present, scattering by the water droplets may be negligible depending upon the density and drop-size distribution of the water droplets relative to the wavelength. In general, the nonscattering assumption is valid for any atmosphere below 10 GHz and up to 50 GHz for nonprecipitating clouds or in the presence of light rain. For the lower and denser layers of the atmosphere, responsible for most of the absorption, local thermodynamic equilibrium is assumed up to 20 km.

For a nonscattering atmosphere in local thermody-

namic equilibrium, the radiative transfer process is simplified, and the brightness temperature T_B is related to the absorptive and emissive processes of the medium by the linearized form of the RTE [*Ulaby et al.*, 1981]:

$$T_B = T_C e^{-\tau(0,\infty)} + \int_0^\infty T(s)\alpha(s)e^{-\tau(0,s)}\,ds \qquad (1)$$

where T_C is the cosmic background emission, commonly assumed as 2.73 K; $T(s)$ is the absolute physical air temperature (in kelvins); s is the spatial position of the emitting air volume (in kilometers); and $\alpha(s)$ is the atmospheric volume absorption coefficient (Np km^{-1}).

Equation (1) states that the sky brightness temperature is the sum of the cosmic background term and of the contributions of the infinite single atmospheric layers along the observed path, both reduced by the absorption of the atmosphere underneath. T_B depends on the vertical profile of the temperature and absorption coefficients; the latter, in turn, corresponds to the vertical distribution and physical properties of the relevant components.

The simplified form of the RTE can be used, according to a direct approach, when the brightness temperature of the atmosphere is calculated from the known vertical distributions of both physical parameters and absorption coefficients. This procedure is commonly adopted in theoretical models making use of radiosonde data.

A second approach, known as the inverse problem, concerns the retrieval of the atmospheric characteristics (physical temperature, total absorption, and composition) from the radiometrically measured values of the brightness temperature. Typical cases when the inverse problem is posed are in meteorology, for deriving the vertical profile of temperature, and in radio propagation, for estimating the atmospheric attenuation. It should be kept in mind, however, that since the direct problem is expressed by an integral equation, the inversion procedure does not usually have a straightforward solution.

3. The Absorption of Nonrainy Atmosphere

The atmosphere is essentially formed by gases and water droplets. At microwave frequencies, absorbing gases are represented by oxygen and water vapor. When only gases are present, the atmosphere is commonly defined as "clear," and the nonscatter assumption is correct. Oxygen and water vapor produce a background level of attenuation increasing with increasing frequency and present a number of critical frequencies where resonant absorption takes place [*Gibbins*, 1988].

The microwave absorption spectrum of oxygen has a complex resonance centered around 60 GHz, extending from 50 to 70 GHz, and a single weaker line at 118.8 GHz. The oxygen concentration in the atmosphere being practically constant, the oxygen absorption depends only on temperature and pressure profiles, and its calculation is rather simple, at least up to 40 GHz.

Water vapor absorption results from the superposition of two terms, one linearly related to the water density and the other a quadratic function of the density. In the microwave and millimeter-wave regions, there is a weak absorption line at 22.235 GHz and much stronger lines at 183.3 and 324.4 GHz. Most of the transitions occur in the infrared region, with hundreds of lines whose low-frequency pressure-broadened wings combine to produce observable effects in the microwave region. It should be noted that for frequencies far from the line centers, the water vapor line shapes are rather uncertain and that estimating vapor absorption in the windows between the peak lines is not straightforward. Clear-sky attenuation is then calculated as the sum of the resonance peaks and of the continua caused by both the wings of the oxygen line at 60 GHz and of all the lines of the water vapor.

An additional absorption continuum, monotonically increasing with frequency, is contributed by liquid water which can occur in the atmosphere, other than the large raindrops, in the form of small suspended droplets of small radius (below 50 μm), contained in liquid clouds and fog. For nonprecipitating clouds the nonscatter assumption is valid up to about 50 GHz. Ice crystals and hail are not considered, since its absorptive effects are negligible. In a nonrainy nonscattering atmosphere, the total attenuation can, in general, be expressed as the sum of the contributions of oxygen, vapor, and cloud liquid water.

4. Radiometric Retrieval of Atmospheric Water Contents

The radiometric brightness temperature can be expressed in terms of attenuation by introducing the quantities

$$T_{mr} = \frac{\int_0^\infty T(s)\alpha(s)e^{-\tau(0,s)}\,ds}{\int_0^\infty \alpha(s)e^{-\tau(0,s)}\,ds} \quad (2)$$

defined as the atmospheric mean radiating temperature (kelvins) [*Wu*, 1979], and

$$\tau(0, \infty) = \int_0^\infty \alpha(s)\,ds \quad (3)$$

defined as optical depth or atmospheric opacity (neper).

If the opacity is small ($\tau(0, \infty) \ll 1$), that is, for low values of the path attenuation, (1) may be written in the well-known simplified form

$$\tau(f) = 4.343 \ln [(T_{mr}(f) - T_C)/(T_{mr}(f) - T_B(f))] \quad (4)$$

that is, the equation commonly used to convert the radiometrically measured brightness temperature into the path attenuation, and represents the simplest inversion of the RTE. Equation (4) should be used, however, for low values of the path attenuation. As the latter increases, in fact, the radiometer measures values of brightness temperature closer and closer to the atmospheric effective radiating temperature, thus leading to a saturation effect.

The mean radiating temperature T_{mr} summarizes the information on the vertical profile of the atmospheric physical properties and depends on frequency and on the local physical and climatological parameters. The use of this single constant to replace a meteorologically varying profile does not appreciably affect the accuracy up to 50 GHz and for sky brightness temperatures lower than some 100 K, that is, in practice, in the absence of rain. Typical rms error value of the mean radiating temperature estimated using long-term radiosonde profiles is about 5 K [*Basili et al.*, 1994].

The vertical distribution of the response in terms of brightness temperature is described by the weighting functions, which express the relative contribution to the brightness increment due to the individual components at any level. A satisfactory simplification is possible, making reference to the integrated precipitable water vapor V and the integrated liquid water L along the considered path, both expressed in millimeters or kg m^{-2}, which in a first approximation can be assumed proportional to the radiometric brightness temperatures when the respective weighting functions are constant with the height [*Westwater et al.*, 1990].

The atmospheric attenuation in the absence of rain can be expressed as the sum of the oxygen absorption and of two terms proportional to the integrated content of the water vapor V and liquid water L, through the relevant mass absorption coefficients. Thus estimates of the two quantities V and L are obtainable from radiometric measurements of the path attenuation at two frequencies, chosen in such a way that the emitted radiation is particularly sensitive to water vapor at one of the frequencies and to liquid water content at the other.

Considering a dual-channel radiometer with one frequency sensitive to the water vapor and the other to the liquid, the following equation system yields [*Westwater and Guiraud*, 1980]

$$\begin{aligned} V &= a_0 + a_1\tau_1 + a_2\tau_2 \\ L &= b_0 + b_1\tau_1 + b_2\tau_2 \end{aligned} \quad (5)$$

where a_i and b_i are the linear statistical inversion coefficients and τ_i are the attenuations at the two frequencies measured by the radiometer through (4). The inversion coefficients, which depend on frequency and temperature, summarize the microwave physical properties of the atmosphere and are usually estimated from radiosonde data on a statistical basis by the use of theoretical models.

Proper choice of the two frequency lines are on one of the shoulders of the vapor peak, at 22.235 GHz as the lower line and the large 30 to 36 GHz water window as the higher one. In general, the larger the difference in terms of absorption of the two components at the two frequencies, the better the accuracy of the retrieval.

The radiometric retrieval of V and L performs well as far as the former is concerned, as shown by comparison with radiosonde observations. However, inaccuracies arise for the liquid content L, due to both its tight dependence on the unknown local temperatures and to the possible involvement of scattering processes. Since measurements of liquid are not reliable even with radiosonde sensors, this parameter must be considered with great caution [*Westwater*, 1978].

5. Experimental Setup

Ground-based radiometric measurements of the sky brightness temperature have been carried out in Italy continuously for 4 years, from September 1992 to August 1996, at the very south side of Rome, in a temperate zone, at 15 km from the sea and subject to

Table 1. WVR-1000 Radiometer Specifications

Specifications	Value
Operating frequencies	23.8–31.4 GHz
Viewing angle	all sky
Antenna beam width	5.0°
Sidelobes	< −25 dB
Gain	31–33 dBi
Sampling time	145 s
Integration time	5 s
Resolution	0.2 K
Accuracy	0.5 K
Wide dual sideband	400 mHz

marine breeze regime and urban environment influence.

The radiometer is a dual-channel, total power, portable type, the model WVR-1000 manufactured by the Radiometrics Corporation, Boulder, Colorado. Its main technical features are summarized in Table 1.

The radiometer operates at 23.8 GHz, near the weak vapor resonant line, and at 31.4 GHz, within the almost transparent window region of liquid water. The radiometer is controlled by a specific software package, and the presence of a RS-232 port allows remote control and data transmission. An elevation mirror controlled by a step-motor allows us to observe all sky portions. A blower system blows air across the window cover to prevent the formation of dew and the accumulation of water on the radome. The instrument can work continuously in unattended mode in almost all weather conditions.

Regular calibration is provided by the tipping-curve method. Calibration of the receiver gain is accomplished using a calibrated Gunn noise diode, which is in turn calibrated by both tipping curves and external liquid nitrogen target. Blackbody source at a known ambient temperature is used to determine the gain and offset of the receiver. This gain calibration is then transferred to the noise diode injection outputs in both channels for future nontipping receiver gain measurements. The stability of the noise diode is maximized by thermally stabilizing the noise diode mount to several hundredths of a degree.

6. Data Preprocessing

Radiometric observations, acquired at a 145-s sample rate, have been edited in different ways to check reliability. Although the major part of the data have satisfactory quality, several natural or instrumental types of outliers might occur, which can arise from the presence of liquid, ice, or snow on the antenna window, spurious electromagnetic signals, calibration drift in the receiver, or errors due to the data transmission system [*Fionda et al.*, 1991]. To detect and eliminate unreliable values, an accurate inspection of daily time series plots of T_B, as well as the check of unlikely pairs of brightness temperature at the two frequencies in the scatterplots, have been performed. The theoretical relationship between the two frequencies was used as a "true" reference, as from the application of theoretical models to a long-term data set of radiosonde profiles, collected twice a day from the Italian Air Force Service, some 15 km apart, from 1981 to 1994.

Records showing outliers at either channel have been entirely disregarded, as well as those acquired during rainy events, identified by a tipping-bucket rain gauge operated close to the radiometer. Additional information to clarify doubtful events has been also used from other instruments operating in the same station: laser ceilometer detecting the cloud base height, standard meteorological setup giving surface pressure, air temperature, and humidity, and from the logbook of daily visual observations of the sky.

The amount of data removed was about 2% of the total data set, the large majority due to rain events. No significant interruption of the acquisition occurred, except for a few short periods accounting for some 2% of the total observation time.

Notwithstanding these checks, some events show very high values of brightness temperature, likely caused by either heavy rain-bearing clouds or suspended bulks of raindrops, which are sensed by the radiometer but not measured by the ground-based rain gauge. The values of T_{mr} used in the calculations are 276.39 and 272.98 K, at 23.8 and 31.4 GHz, respectively, calculated applying theoretical absorption models [*Liebe*, 1989; *Rosenkranz*, 1988] on the long-term radiosonde data, from which also the inversion coefficient for the retrieval of atmospheric water contents V and L have been derived [*Barbaliscia et al.*, 1994].

7. Statistics of Sky Brightness Temperature

Statistical analysis has been carried out for the entire 4-year period, as well as for seasons and single average months. Figure 1 shows the cumulative dis-

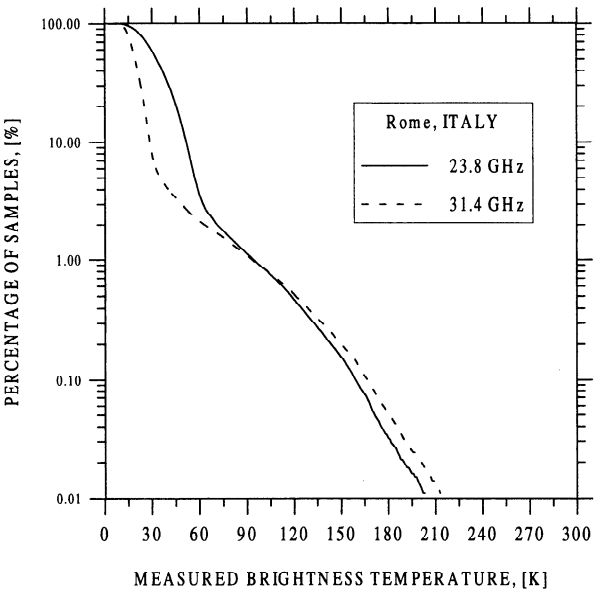

Figure 1. Cumulative distributions of zenith brightness temperature at 23.8 and 31.4 GHz (average of 4 years).

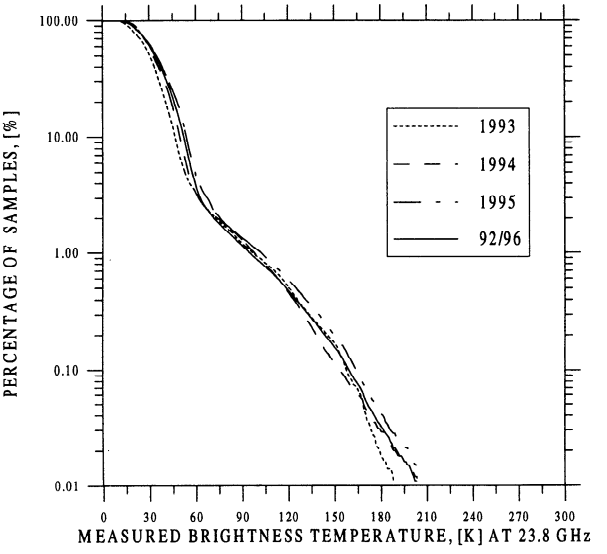

Figure 2. Annual cumulative distributions of zenith brightness temperature at 23.8 GHz.

tribution functions of the brightness temperatures measured along zenithal path, at the two frequencies, for the entire period of 4 years.

Two regions can be identified, above and below the 1% of the year (90 hours), where the two channels cross around 90 K. Grossly speaking, this threshold separates the time when heavy rain-bearing clouds occur from the much longer time during which the sky is lightly cloudy or clear. The latter condition, however, occurs for times much shorter, around 50% of the time.

During some 99% of the time, however, the lower 23.8-GHz channel shows higher response with respect to the 31.4-GHz one, more sensible to liquid, because clouds are very light or absent and the water vapor absorptive process is dominant. The reverse happens for 1% of the time, when clouds are dense enough to make the T_B at 31.4 GHz higher than the 23.8-GHz one. Just for an observation time less than 10 hours, events occur with brightness temperature so high (>150 K) that they imply the presence of bulk of water aloft, as mentioned before.

For both the channels a change of slope is evident: around 60 K (3%) for the vapor line (23.8 GHz) and 30 K (5%) for the water line (31.4 GHz). As a first indication of the status of the sky, these thresholds can be seen as the borders between clear and cloudy sky, for the two frequencies [*Barbaliscia et al.*, 1993].

The year-to-year variability, reported in Figures 2 and 3, appears limited for both channels, implying that few years of measurements are statistically representative. Very limited variations are, however, confined to small time fractions (<1%). Mean and standard deviation show an annual variability of 5 and 2 K, respectively, on both channels. In Table 2 the comparison is presented with the theoretical values

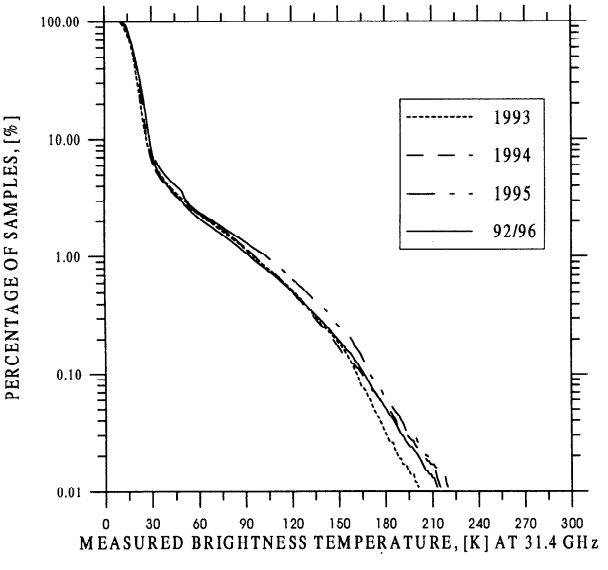

Figure 3. Annual cumulative distributions of zenith brightness temperature at 31.4 GHz.

Table 2. Mean and Standard Deviation of Calculated and Measured Brightness Temperatures

Source	Period	Mean	s.d.	Number of Points
		23.8 GHz		
Radiometer	1993	31.8	15.61	160,692
Radiometer	1994	34.8	15.00	199,500
Radiometer	1995	36.5	16.69	204,046
Radiometer	1992–1996	35.4	15.71	751,596
RAOB	1981–1994	36.6	15.43	7,063
		31.4 GHz		
Radiometer	1993	21.0	14.35	160,692
Radiometer	1994	21.9	14.16	199,500
Radiometer	1995	22.5	15.27	204,046
Radiometer	1992–1996	22.2	14.10	751,596
RAOB	1981–1994	24.3	16.81	7,063

RAOB, radiosonde observation.

Table 3. Monthly Percentiles of Brightness Temperature Distributions at 23.8 and 31.4 GHz

	T_B (23.8 GHz), K			T_B (31.4 GHz), K		
	10%	1%	0.1%	10%	1%	0.1%
Jan.	38.8	99.3	143.0	26.4	102.0	159.0
Feb.	35.9	109.0	153.0	25.8	112.0	167.0
March	35.4	102.0	176.0	23.9	104.0	180.0
April	43.1	111.0	163.0	28.8	115.0	169.0
May	46.8	88.8	156.0	27.4	87.2	169.0
June	53.7	79.4	162.0	29.3	74.1	172.0
July	56.3	65.4	129.0	29.7	40.4	133.0
Aug.	57.2	72.2	173.0	29.2	53.2	177.0
Sept.	57.7	106.0	182.0	31.9	101.0	191.0
Oct.	49.6	81.4	145.0	27.4	69.5	148.0
Nov.	42.1	83.4	161.0	24.0	82.3	165.0
Dec.	44.9	102.0	162.0	32.0	104.0	169.0
Year	52.2	93.7	160.0	28.8	92.6	168.0
Worst	57.7	111.0	182.0	32.0	115.0	191.0
Best	35.4	65.4	129.0	23.9	40.4	133.0

calculated on long-term radiosonde data, which shows good agreement between calculated and measured brightness temperatures.

The atmospheric emission on a seasonal basis is shown in Figure 4, as winter (December–February) and summer (July–September). Vapor density, being higher in summer, makes the emission at 23.8 GHz increase with respect to winter. At 31.4 GHz the emission is once again stronger in summer because of few events of heavy rain-bearing clouds and tends to slightly prevail over winter also for very long times, notwithstanding the higher cloud coverage, because of the higher vapor density. The intersections between the curves occur now at different values because of climatic variability of vapor and clouds. In winter the intersection point is around 5% of the time at some 45 K, while for the summer this value decreases to 2% at about 70 K.

The influence of climate is also evident on a monthly basis, as reported in Table 3 and Figures 5 and 6. It can be noted that as a difference to the case of rain, no month appears to behave as the "worst"

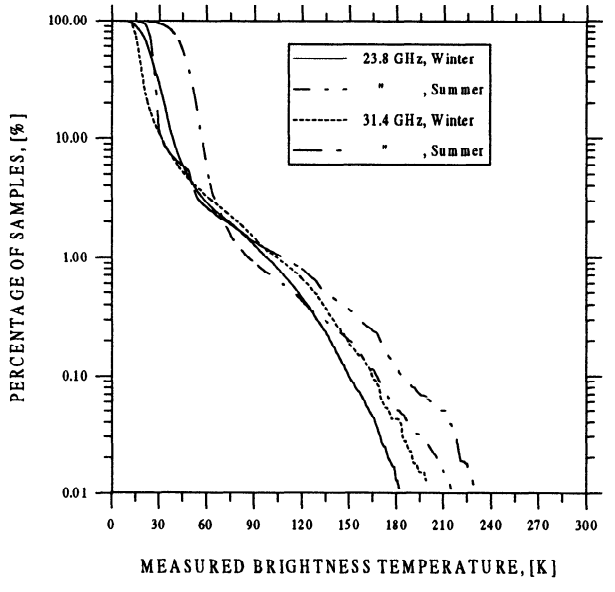

Figure 4. Seasonal cumulative distributions of zenith brightness temperature.

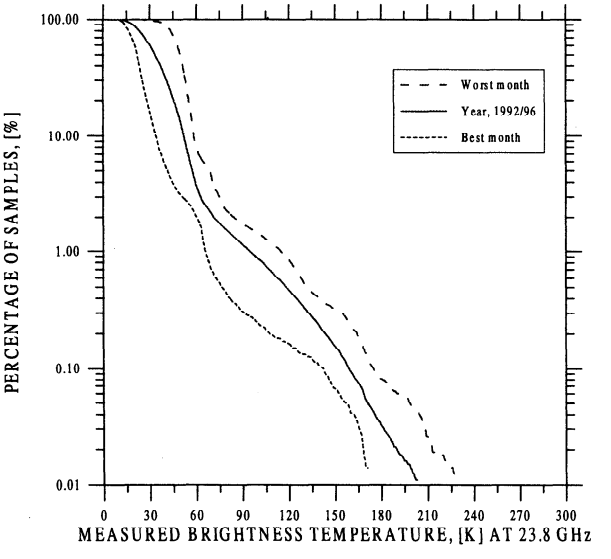

Figure 5. Monthly cumulative distributions of zenith brightness temperature at 23.8 GHz.

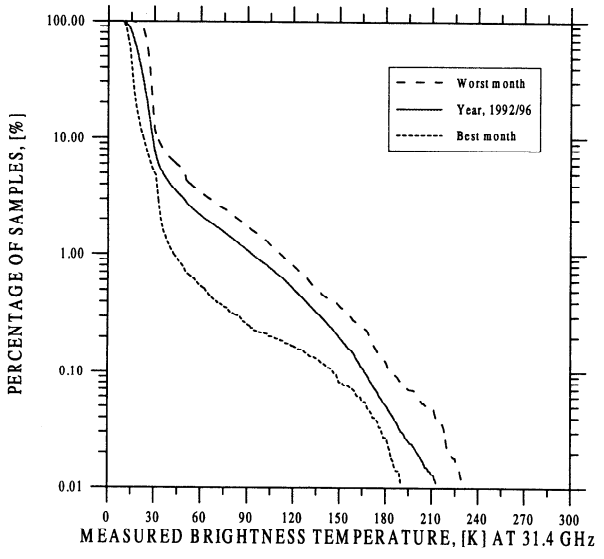

Figure 6. Monthly cumulative distributions of zenith brightness temperature at 31.4 GHz.

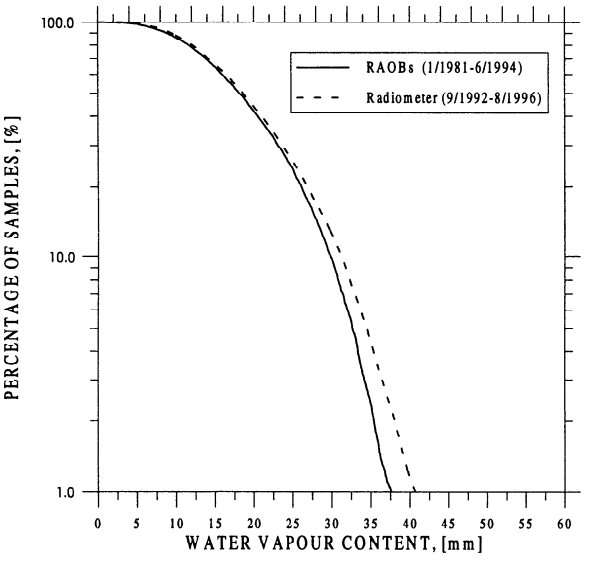

Figure 7. Cumulative distributions of retrieved and calculated integrated water vapor V.

and "best" month, although in July the sky brightness is much lower with respect to April and September.

At 23.8 GHz the thermal response of water vapor makes the spread larger and summer months clearly prevail, while at 31.4 GHz the larger cloud coverage in winter partly compensates for the vapor effect in summer, at least for the 90% of the time.

8. Statistics of the Integrated Water Content

The atmospheric water contents, both the precipitable water vapor and the liquid water, are of paramount relevance to many atmospheric processes. The knowledge of the features of these parameters is useful in several fields: climate, weather forecasting, remote sensing, radio astronomy, and satellite communications.

As mentioned in section 4, dual-channel radiometric observations can provide estimates of the integrated water vapor V and liquid L contents, according to (4) and (5). The accuracy of the retrieval depends on several factors and is quite reliable for the vapor, while caution should be used for the liquid, especially insofar as high values are concerned.

The radiometrically retrieved values of V have been compared with the corresponding long-term data, calculated applying atmospheric emission models to long-term radiosonde profiles. Although the data sets do not refer to the same period (1980 to June 1994 for the radiosonde) and site (15 km apart), the comparison, reported in Figure 7, shows good agreement for 99% of samples.

At 1% the difference is only about 5 mm, with a light overestimation of the radiometric values. Discrepancies arise from percentage less than 1% with vapor greater than about 35 mm, likely due to spatially limited events.

Statistical distributions of V and L are reported in Figures 8 and 9, for the full period and the mean of worst and best months, and in Table 4 for monthly detail. The vapor distribution is dominated by the thermal cycle, where summer months clearly prevail over winter in about 1% of samples, with a month-to-month variability limited within 20 mm. Some changes are found below, for a few events when local meteorology factors prevail.

As far as the total liquid is concerned, no differences at all are present for the 90%, while the spread increases markedly below 10%, where the contribution of dry summer months is much less than the others, April and September, in particular. Percentile level analysis helps to confirm the behavior of water contents over the year. For the vapor total content, depicted in Figure 10, the thermal response is confirmed up to 3% of the time, and seasonal fluctuations start to occur from 1%, showing peaks in spring and

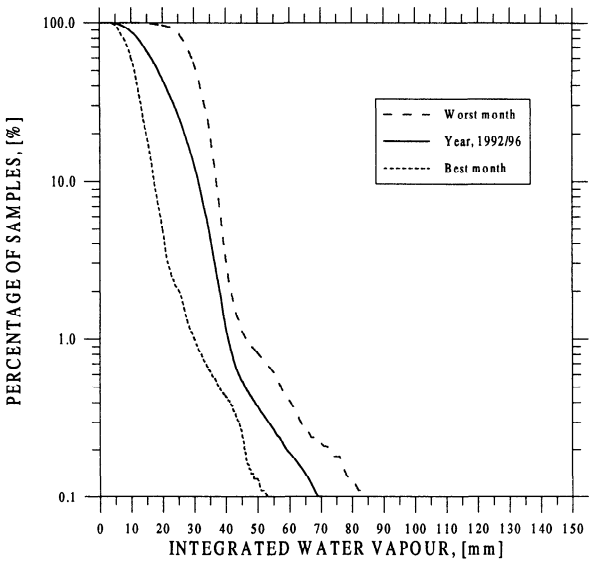

Figure 8. Annual and extreme months cumulative distributions of integrated water vapor content V.

late summer, while "dry windows" can be identified in July and October as well as in the winter period.

A similar behavior, even more pronounced, is shown by the total liquid L, as in Figure 11, with the difference that no cycle at all can be observed above some 10%. Although caution should be used for high values of L, taking into account the statistical instability, the above features seem consistent and are substantially in agreement with the climatic features of the zone.

Table 4. Monthly Percentiles of Cumulative Distributions of Total Vapor and Liquid Water Contents

	Water Vapor, mm			Liquid Water, mm		
	10%	1%	0.3%	10%	1%	0.3%
Jan.	20.1	30.0	44.1	0.13	1.15	2.30
Feb.	17.2	35.2	49.2	0.09	1.54	2.70
March	18.8	32.6	54.0	0.10	1.40	2.80
April	22.1	40.2	57.0	0.16	1.88	3.30
May	26.1	34.0	44.2	0.10	0.90	2.10
June	31.9	39.1	48.5	0.11	0.60	1.90
July	35.2	40.6	44.2	0.11	0.28	0.87
Aug.	36.3	43.0	60.0	0.10	0.81	3.00
Sept.	35.0	46.3	63.0	0.14	1.47	3.10
Oct.	29.9	40.3	52.0	0.11	1.09	2.20
Nov.	25.2	45.5	64.0	0.13	1.67	2.80
Dec.	22.7	38.6	53.0	0.22	1.65	2.70
Year	31.0	40.5	54.0	0.11	1.28	2.60
Worst	36.3	46.3	64.0	0.22	1.88	3.30
Best	17.2	30.0	44.1	0.11	0.28	0.87

The analysis of the dependence of atmospheric water contents upon any daily cycle over the hours of the day has been carried out as well and is reported, in terms of percentile levels, in Figures 12 and 13, for the total V and total L, respectively. Differences among the hours of the day appear only for very low probabilities, especially for the liquid. No physical

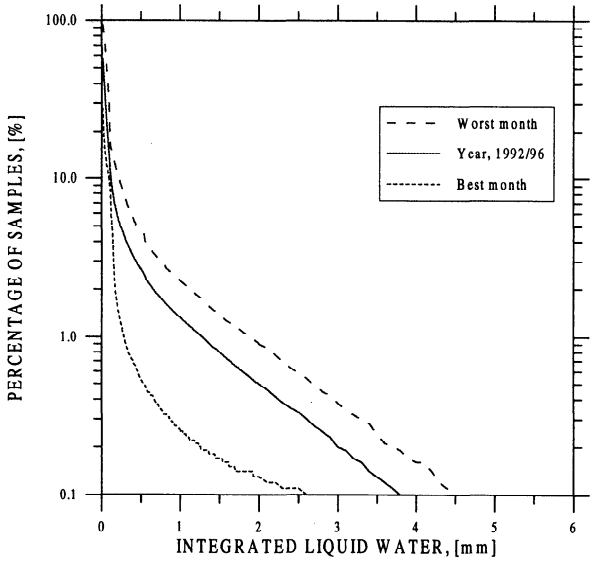

Figure 9. Annual and extreme months cumulative distributions of integrated liquid water content L.

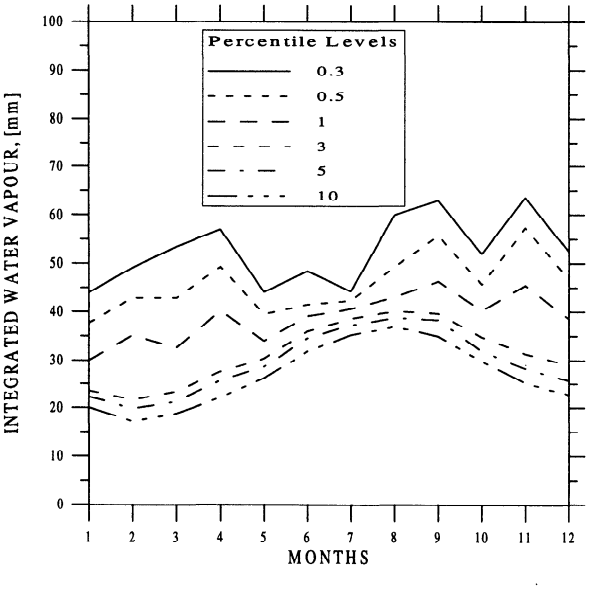

Figure 10. Monthly percentiles of integrated water vapor content V.

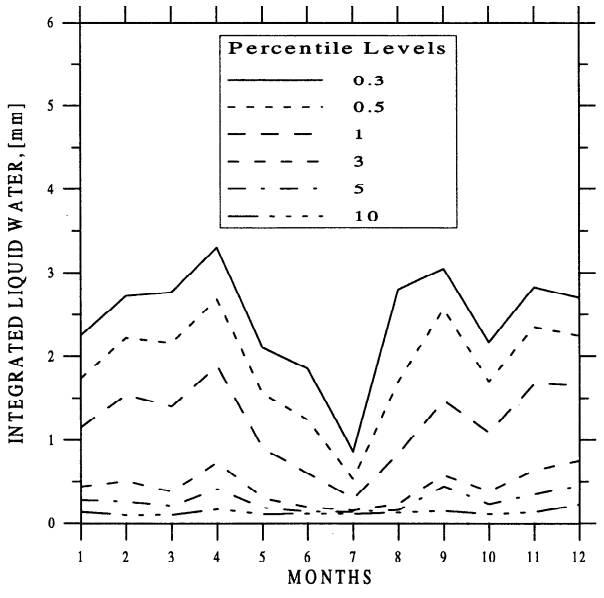

Figure 11. Monthly percentiles of integrated liquid water content L.

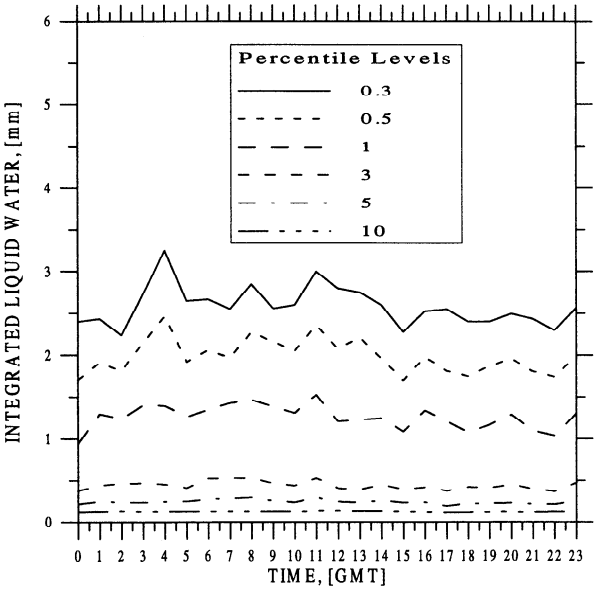

Figure 13. Daily percentiles of the integrated liquid water content L.

consistency and correlation with meteorological processes and factors appears evident.

9. Conclusions

Four years of radiometric measurements of the sky brightness temperature are presented, together with the corresponding values of the atmospheric water contents, as retrieved from inversion of radiometric attenuation. Cumulative statistics are analyzed showing the influence of the two water phases on the radiometric frequencies and the dependence of the atmospheric thermal emission upon seasonal climatic features. Water vapor content, in particular, shows a tight correlation with air temperature, while liquid cloud content has a more random behavior, more similar to rain formation, so that its effect varies markedly with its features, the water total content, however, being the dominant one. Some degree of correlation has also been found between the ratio of radiometric brightness at the two frequencies and the status of the sky. The year-to-year variability is shown to be really limited, although the observation period is too short to conclude that few years of data can be assumed as statistically representative on a long time basis. Daily statistics have been performed as well, from which no daily cycle appears dominant, except for few extreme events where, however, no physical and meteorological modeling can be attempted.

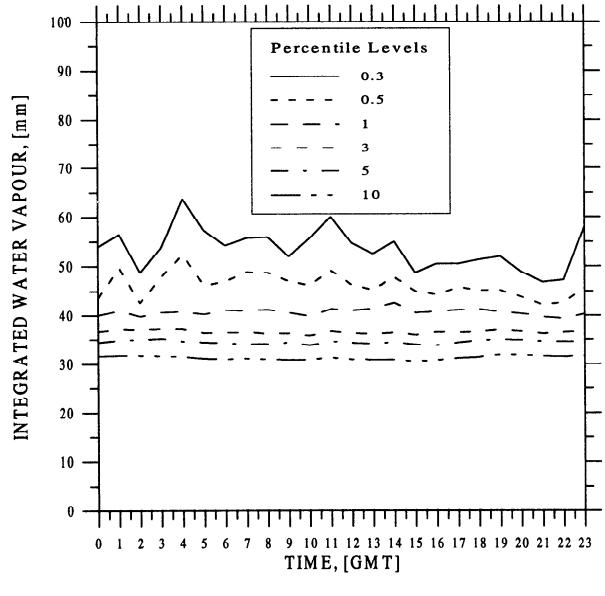

Figure 12. Daily percentiles of the integrated water vapor content V.

Acknowledgments. The authors thank the Meteorological Service of the Italian Air Force for radiosonde data, as well as M. Boumis for help in processing radiosonde data and A. Capitanio and F. Consalvi for assistance in instrumental keeping.

References

Barbaliscia, F., E. Fionda, and P. G. Masullo, Characterization of the status of the sky by means of radiometric observations at 20/30 GHz, in *Proceedings of the 1993 Symposium on Radio Propagation (ISRP'93)*, pp. 210–213, Chin. Inst. of Electron., Radio Propag. Soc., Beijing, 1993.

Barbaliscia, F., L. Guerriero, G. Schiavon, and D. Solimini, Space-Earth absorption in the absence of rain: Radiometric inversion coefficients for Italy, *Eur. Trans. Telecommun.*, *5*(6), 51–57, 1994.

Basili, P., P. Ciotti, and E. Fionda, Comparison of algorithms for the retrieval of water vapour, cloud liquid and atmospheric attenuation by microwave radiometry, in *Proceedings of PIERS 1994*, pp. 571–574, Euro. Space Agency, ESTEC, Noordwijk, Netherlands, 1994.

Fionda, E., M. J. Falls, and E. R. Westwater, Attenuation statistics at 20.6, 31.65 and 52.85 GHz derived from emission measurements by ground-based microwave radiometers, *IEE Proc., Part H*, *138*(1), 46–50, 1991.

Gibbins, C. J., The effects of the atmosphere on radio wave propagation in the 50–70 GHz frequency band, *J. Inst. Electron. Radio Eng.*, *58*(6) suppl., S229–S240, 1988.

Liebe, H. J., MPM—An atmospheric millimeter-wave propagation model, *Int. J. Infrared Millimeter Waves*, *10*, 631–650, 1989.

Rosenkranz, P. W., Interference coefficients for overlapping oxygen lines in air, *J. Quant. Spectrosc. Radiat. Transfer*, *39*, 287–297, 1988.

Ulaby, F. T., R. K. Moore, and A. K. Fung, *Microwave Remote Sensing: Active and Passive*, vol. 1, *Microwave Remote Sensing Fundamentals and Radiometry*, Addison-Wesley, Reading, Mass., 1981.

Westwater, E. R., The accuracy of water vapor and cloud liquid determination by dual-frequency ground-based microwave radiometry, *Radio Sci.*, *13*(4), 677–685, 1978.

Westwater, E. R., and F. O. Guiraud, Ground-based microwave radiometric retrieval of precipitable water vapor in the presence of clouds with high liquid content, *Radio Sci.*, *15*(5), 947–957, 1980.

Westwater, E. R., J. B. Snider, and M. J. Falls, Ground-based radiometric observations of atmospheric emission and attenuation at 20.6, 31.65, and 90.0 GHz: A comparison of measurements and theory, *IEEE Trans. Antennas Propag.*, *38*, 1569–1580, 1990.

Wu, S. C., Optimum frequencies of a passive microwave radiometer for tropospheric path-length correction, *IEEE Trans. Antennas Propag.*, *27*, 233–239, 1979.

F. Barbaliscia, E. Fionda, and P. G. Masullo, Fondazione Ugo Bordoni, viale Europa 190, 00144 Roma, Italy. (e-mail: fbarba@fub.it; ermanno@fub.it; giorgio@fub.it)

(Received March 7, 1997; revised August 19, 1997; accepted September 19, 1997.)